

Evolution of 3D Boson Stars with Waveform Extraction

Jayashree Balakrishna¹, Ruxandra Bondarescu², Gregory Daues³, F. Siddhartha Guzmán⁴ and Edward Seidel^{5,6,7}

¹Harris-Stowe State University, St. Louis, MO USA.

²Cornell University, Ithaca, NY USA.

³National Center for Supercomputing Applications, Urbana, IL USA.

⁴Instituto de Física y Matemáticas, Universidad Michoacana de San Nicolás de Hidalgo. Edificio C-3, Cd. Universitaria. C. P. 58040 Morelia, Michoacán, México.

⁵Center for Computation and Technology, 302 Johnston Hall, Louisiana State University, Baton Rouge, LA 70803.

⁶Department of Physics and Astronomy, 202 Nicholson Hall, Louisiana State University, Baton Rouge, LA 70803.

⁷Max Planck Institut für Gravitationsphysik, Albert Einstein Institut, Am Mühlenberg 1, 14476 Golm, Germany.

PACS numbers: 04.40.-b, 04.25.Dm, 04.30.Db

Abstract.

Numerical results from a study of boson stars under nonspherical perturbations using a fully general relativistic 3D code are presented together with the analysis of emitted gravitational radiation. We have constructed a simulation code suitable for the study of scalar fields in space-times of general symmetry by bringing together components for addressing the initial value problem, the full evolution system and the detection and analysis of gravitational waves. Within a series of numerical simulations, we explicitly extract the Zerilli and Newman-Penrose scalar Ψ_4 gravitational waveforms when the stars are subjected to different types of perturbations. Boson star systems have rapidly decaying nonradial quasinormal modes and thus the complete gravitational waveform could be extracted for all configurations studied. The gravitational waves emitted from stable, critical, and unstable boson star configurations are analyzed and the numerically observed quasinormal mode frequencies are compared with known linear perturbation results. The superposition of the high frequency nonspherical modes on the lower frequency spherical modes was observed in the metric oscillations when perturbations with radial and nonradial components were applied. The collapse of unstable boson stars to black holes was simulated. The apparent horizons were observed to be slightly nonspherical when initially detected and became spherical as the system evolved. The application of nonradial perturbations proportional to spherical harmonics is observed not to affect the collapse time. An unstable star subjected to a large perturbation was observed to migrate to a stable configuration.

1. Introduction

Spin zero particles play an important role in particle physics and cosmological models. Studies of the early universe have suggested that these types of bosons may have played significant roles in determining its history. These roles range from the inflaton, a scalar field that could be responsible for the inflation of the universe at very early stages [1], up to the quintessence, which is a scalar field used to model the dark energy component of the current universe [2]. Bosonic particles could come together through some kind of a Jeans instability mechanism to form gravitationally bounded objects such as boson stars (complex scalar field) or oscillatons (real scalar field) [3]. These objects would be held together by the balance between the attractive force of gravity and the dispersive effects of the uncertainty principle (the wave character of the scalar field). Boson stars in the Newtonian regime have been considered as candidates for dark matter in the context of galactic halos [4]. In the strong field regime these stars have been shown to be reliable models for the supermassive objects in the center of some galaxies [5] and it has been shown that they may play the role of black hole candidates [6].

If these objects exist, the process of formation could include multipolar components of the gravitational field that should transform into gravitational waves. Due to post-formation perturbations, boson stars could generate gravitational radiation. The head-on collision of two boson stars has been investigated previously as a source of gravitational waves [7]. When two boson stars collide to form a black hole very little scalar radiation is emitted and most of the energy is lost in gravitational radiation [7]. Ryan [8] has studied the scenario of a boson star of mass greater than several M_{\odot} coalescing with a particle such as a small black hole. He finds that this system can generate a signal detectable by a gravitational wave interferometer such as LIGO and future generation gravitational wave detectors. Recently, Kesden *et al.* [9] have studied the infall of a stellar mass compact object onto a supermassive boson star and studied an approximate gravitational wave signal, which could point to differences between supermassive horizonless objects (like those in Ref. [5]) and supermassive black holes in the center of galaxies.

The detection of boson stars, either as compact objects or as bricks of the dark matter component, necessitates studying their behavior under general nonspherical perturbations. Extracting their particular gravitational wave signatures, under general perturbations, requires a fully general relativistic 3D code. Boson stars also have an important role in the field of numerical relativity aside from their relevance to astrophysics. The performance of long-term stable 3D simulations of systems with general symmetry and construction of a full gravitational wave signal is a timely and challenging problem in general relativity. Boson stars are amenable to stable 3D simulation due to their smooth surface and the absence of singularities, offering a suitable testbed for the field.

The properties of spherically symmetric boson stars are well studied in the literature [10, 11, 12, 13, 14, 15, 16, 17]. Critical solutions and spherically symmetric boson

stars brought to the threshold of black hole formation were studied by Hawley and Choptuik in Ref. [18]. They performed a comparison between radial quasinormal mode frequencies of boson stars calculated via perturbation theory and those of the numerically constructed critical solutions. An investigation of the properties of boson stars beyond the spherically symmetric case was performed by Yoshida *et al.* [19]. The authors calculate the quasinormal mode frequencies corresponding to nonradial pulsations of a boson star. They perform a linear expansion about the spacetime of a spherically symmetric static boson star configuration according to the decomposition into tensor spherical harmonics developed by Regge and Wheeler. Their results consist of a series of complex quasinormal mode frequencies for even parity perturbations for three models of stable, critical, and unstable boson star configurations. These modes are damped in a short time because of large imaginary parts of the frequencies.

The focus of this paper is the nonspherical perturbation problem of spherical boson stars and the gravitational wave signals generated by such systems. The simulations shown here are performed using the fully general 3D simulation code presented in [20], which is based on the Cactus Computational Toolkit [21]. The existence of the rapidly damping quasinormal modes predicted by Yoshida *et al.* is confirmed numerically. Both the Zerilli and the Newman-Penrose Ψ_4 gravitational waveforms are fully extracted for the first time for boson stars. The generated waveforms are compared to modefits constructed with the $\ell = 2$ quasinormal mode frequencies calculated by Ref. [19]. After the waveforms are extracted numerically, the energy loss to gravitational radiation is estimated.

In addition to subjecting stars to perturbations proportional to $\ell = 2$ spherical harmonics that allowed the comparison between our waveforms and the frequency spectrum predicted by Ref. [19], we subjected stars to more physical perturbations and studied (1) the collapse of an unstable boson star to a black hole and (2) the migration of a star from the unstable to the stable branch. The collapse of an unstable branch boson star was accelerated by applying a mixture of nonradial and radial perturbations. The apparent horizon was observed to be measurably nonspherical when the horizon formed before the complete relaxation of the nonradial modes. The migration is initiated by applying a radial perturbation that significantly reduces the mass of the star. A nonspherical perturbation is superimposed on the spherical one and the system is evolved. At early times (before a single radial oscillation is complete) the full gravitational wave signal is extracted. The migration process was further followed to track the continuing low frequency radial oscillations of the metric function g_{rr} (lasting hundreds of oscillations of the underlying complex scalar field – a very long time scale simulation).

The paper proceeds by providing a brief overview of the mathematical background that describes the evolution system and the formulation of the initial value problem. Sec. 3.1 discusses the different types of perturbation methods and the different boson star models considered. The results of simulations are then presented in Sec. 3.2 for stable, critical and unstable boson star configurations under small nonradial perturbations. The

collapse of an unstable star to a black hole and the formation of the apparent horizon are subsequently presented in Sec. 3.3. Finally, the migration of an unstable branch boson star to the stable branch under explicit radial and nonradial perturbations is detailed in Sec. 3.4. The results are summarized in the conclusion.

2. Mathematical Background

2.1. General Relativistic Evolution System

The action describing a self-gravitating complex scalar field in a curved spacetime is given by

$$I = \int d^4x \sqrt{-g} \left(\frac{1}{16\pi} R - \frac{1}{2} [g^{\mu\nu} \partial_\mu \Phi^* \partial_\nu \Phi + V(|\Phi|^2)] \right) \quad (1)$$

where R is the Ricci scalar, $g_{\mu\nu}$ is the metric of the spacetime, g is the determinant of the metric, Φ is the scalar field, V its potential of self-interaction, and the geometric units $G = c = 1$ have been used. The variation of this action with respect to the scalar field leads to the Klein-Gordon equation for the complex scalar field, which can be written as

$$\Phi^{;\mu}{}_{;\mu} - \frac{dV}{d|\Phi|^2} \Phi = 0. \quad (2)$$

When the variation of Eq. (1) is made with respect to the metric $g^{\mu\nu}$, the Einstein's equations $G_{\mu\nu} = 8\pi T_{\mu\nu}$ arise, and the resulting stress energy tensor reads

$$T_{\mu\nu} = \frac{1}{2} [\partial_\mu \Phi^* \partial_\nu \Phi + \partial_\mu \Phi \partial_\nu \Phi^*] - \frac{1}{2} g_{\mu\nu} [\Phi^{*,\eta} \Phi_{,\eta} + V(|\Phi|^2)]. \quad (3)$$

In the present manuscript we focus on the free-field case, for which the potential is $V = m^2 |\Phi|^2$, where m is interpreted as the mass of the field.

In order to find solutions to the Einstein-Klein-Gordon system of equations we use the 3+1 decomposition of Einstein's equations, for which the line element can be written as

$$ds^2 = -\alpha^2 dt^2 + \gamma_{ij} (dx^i + \beta^i dt) (dx^j + \beta^j dt) \quad (4)$$

where γ_{ij} is the 3-dimensional metric; from now on latin indices label the three spatial coordinates. The functions α and β^i in Eq. (4) are freely specifiable gauge parameters, known as the lapse function and the shift vector respectively. The determinant of the 3-metric γ is defined as $\gamma = \gamma_{ij} \gamma^{ij}$. Throughout this paper the standard general relativity notation is used. The Greek indices run from 0 to 3 and the Latin indices run from 1 to 3.

The Klein-Gordon equation can be written as a first-order evolution system by first splitting the scalar field into its real and imaginary parts: $\Phi = \phi_1 + i\phi_2$, and then defining eight new variables in terms of combinations of their derivatives: $\Pi = \pi_1 + i\pi_2$

and $\psi_a = \psi_{1a} + i\psi_{2a}$ with $\pi_1 = (\sqrt{\gamma}/\alpha)(\partial_t\phi_1 - \beta^c\partial_c\phi_1)$ and $\psi_{1a} = \partial_a\phi_1$ and similarly ($1 \rightarrow 2$). With this notation the evolution equations become

$$\begin{aligned}\partial_t\phi_1 &= \frac{\alpha}{\gamma^{\frac{1}{2}}}\pi_1 + \beta^j\psi_{1j} \\ \partial_t\psi_{1a} &= \partial_a\left(\frac{\alpha}{\gamma^{\frac{1}{2}}}\pi_1 + \beta^j\psi_{1j}\right) \\ \partial_t\pi_1 &= \partial_j(\alpha\sqrt{\gamma}\phi_1^j) - \frac{1}{2}\alpha\sqrt{\gamma}\frac{\partial V}{\partial|\Phi|^2}\phi_1\end{aligned}\tag{5}$$

and ($1 \rightarrow 2$). On the other hand, the geometry of the spacetime is evolved using the BSSN formulation of the 3+1 decomposition. According to this formulation, the variables to be evolved are $\Psi = \ln(\gamma_{ij}\gamma^{ij})/12$, $\tilde{\gamma}_{ij} = e^{-4\Psi}\gamma_{ij}$, $K = \gamma^{ij}K_{ij}$, $\tilde{A}_{ij} = e^{-4\Psi}(K_{ij} - \gamma_{ij}K/3)$ and the contracted Christoffel symbols $\tilde{\Gamma}^i = \tilde{\gamma}^{jk}\Gamma_{jk}^i$, instead of the usual ADM variables γ_{ij} and K_{ij} . The evolution equations of these new variables are described in Refs. [22, 23]:

$$\partial_t\Psi = -\frac{1}{6}\alpha K\tag{6}$$

$$\partial_t\tilde{\gamma}_{ij} = -2\alpha\tilde{A}_{ij}\tag{7}$$

$$\partial_t K = -\gamma^{ij}D_i D_j \alpha + \alpha\left[\tilde{A}_{ij}\tilde{A}^{ij} + \frac{1}{3}K^2 + \frac{1}{2}(-T^t_t + T)\right]\tag{8}$$

$$\partial_t\tilde{A}_{ij} = e^{-4\Psi}[-D_i D_j \alpha + \alpha(R_{ij} - T_{ij})]^{TF}\tag{9}$$

$$+ \alpha(K\tilde{A}_{ij} - 2\tilde{A}_{il}\tilde{A}_j^l)\tag{10}$$

$$\begin{aligned}\frac{\partial}{\partial t}\tilde{\Gamma}^i &= -2\tilde{A}^{ij}\alpha_{,j} + 2\alpha\left(\tilde{\Gamma}_{jk}^i\tilde{A}^{kj}\right. \\ &\quad \left.- \frac{2}{3}\tilde{\gamma}^{ij}K_{,j} - \tilde{\gamma}^{ij}T_{jt} + 6\tilde{A}^{ij}\phi_{,j}\right) \\ &\quad - \frac{\partial}{\partial x^j}\left(\beta^l\tilde{\gamma}^{ij}_{,l} - 2\tilde{\gamma}^{m(j}\beta^{i)}_{,m} + \frac{2}{3}\tilde{\gamma}^{ij}\beta^l_{,l}\right).\end{aligned}\tag{11}$$

where D_i is the covariant derivative in the spatial hypersurface, T is the trace of the stress-energy tensor (3) and the label TF indicates the trace-free part of the quantity in brackets. The coupling between the evolution of the BSSN variables and the variables describing the evolution of the scalar field is first order. That is, Eqs. (5) are solved using the method of lines with a modified version of the second order iterative Crank-Nicholson (ICN) integrator (see Ref. [24]). After a full time step the stress-energy tensor in Eq. (3) is calculated and used to solve the BSSN evolution equations with an independent evolution loop based on the standard second order ICN [25].

In addition to the formulation of Einstein's equations and the first order form of the Klein-Gordon equation we use certain gauge choices to determine the lapse function of Eq. (4) (the shift vector is zero in all of our simulations). The evolutions presented in Sec. 3.2 were carried out using the 1 + log slicing condition with the lapse given by

$\partial_t \alpha = -2\alpha K$, where K is the trace of the extrinsic curvature. The more dynamic evolutions in Secs. 3.3 and 3.4, black hole formation from boson star collapse and migration of an unstable boson star to the stable branch, used a combination of both maximal and $1 + \log$ slicing. Maximal slicing was enforced using a K-driver [26].

In order to set up the correct scaled quantities to be evolved we use dimensionless variables. For an equilibrium configuration the complex scalar field has a time dependence of the form $\Phi(r, t) = \phi(r)e^{i\omega_0 t}$. This implies that the stress energy components given in Eq. (3) and therefore the geometry of the spacetime have to be time-independent, whereas the field is oscillating with the characteristic frequency ω_0 that depends on the central value of the field $\phi(0)$. This characteristic frequency ω_0 together with the mass of the boson m provide the natural dimensionless units,

$$\begin{aligned} r_{\text{code}} &= mr/M_{\text{Pl}}^2, & t_{\text{code}} &= \omega_0 t, \\ \phi_{\text{code}} &= \frac{\sqrt{4\pi}}{M_{\text{Pl}}} \phi, & \alpha_{\text{code}} &= \alpha \frac{m}{M_{\text{Pl}}^2 \omega_0}, \end{aligned} \quad (12)$$

which are the ones used within the present analysis. For further code details refer to Ref. [20].

2.2. Formulation of the Initial Value Problem (IVP)

Performing numerical simulations in the 3+1 ADM formulation requires the construction of valid initial data on some constant time hypersurface. This task entails finding a numerical solution to the four nonlinear coupled elliptic equations given by the Hamiltonian and momentum constraint equations of the ADM formalism. Finding solutions for physically interesting systems that are not highly symmetric can be very difficult and computationally expensive. The presence of matter terms as a source increases the complexity even further.

We consider the case of time symmetric initial data where the extrinsic curvature $K_{ij} = 0$ on the initial hypersurface ($t = 0$) and a background scalar field configuration $\phi(r)$ is assumed. Under the condition of time symmetry the equations decouple and it becomes sufficient to solve only one nonlinear elliptic equation, i.e., the Hamiltonian constraint. For a massive complex scalar field the constraint equation takes the form

$$R = 16\pi\rho(\gamma_{ij}, \phi, \Pi) \quad (13)$$

where the scalar curvature is $R = \gamma^{ij} R_{ij}$ and ρ is the energy density. Using the York formalism, we introduce a conformal factor Ψ that relates the actual 3-metric γ_{ij} to an initial guess $\tilde{\gamma}_{ij}$ through the relation $\gamma_{ij} = \Psi^4 \tilde{\gamma}_{ij}$. Under this transformation the scalar curvature is given by

$$R = \frac{1}{\Psi^4} \tilde{R} - \frac{8}{\Psi^5} \tilde{\Delta} \Psi \quad (14)$$

In the standard York procedure, all the terms within the energy density are transformed uniformly using the relation $\rho = \Psi^{-8} \tilde{\rho}$. This transformation would require finding a

new bosonic field configuration corresponding to the new energy density ρ , which is a nontrivial problem. We circumvented this difficulty by explicitly writing the dependence of the energy density on the metric functions. The conformal transformation is applied term by term within ρ , leaving the scalar field configuration unchanged. On the initial hypersurface the Hamiltonian constraint (Eq. (13)) can be rewritten as the nonlinear elliptic equation

$$\frac{1}{\Psi^4} \tilde{R} - \frac{8}{\Psi^5} \tilde{\Delta} \Psi = 16\pi \left[\frac{1}{2} \frac{1}{\Psi^{12} \tilde{\gamma}} \Pi_1^2 - \frac{1}{2} \frac{1}{\Psi^4} \tilde{\gamma}^{ij} \phi_{1,i} \phi_{1,j} - \frac{1}{2} m^2 \phi_1^2 + (\phi_1 \mapsto \phi_2) \right] \quad (15)$$

We start with an initial guess and then solve the constraint equation for the conformal factor Ψ . This formulation of the IVP problem was first used in Balakrishna's Ph.D. thesis for a variety of physical situations related to boson stars [7].

3. Evolution of Perturbed Boson Stars

Table 1 details the four different boson star configurations studied in this paper. The mass profile plot in Fig. 1 shows the mass versus central field density $\phi(0)$. All configurations listed in Table 1 have negative binding energy ($M < Nm$). Model 1 is a star on the stable branch, Model 2 is a critical boson star, and Models 3a and 3b both lie on the unstable branch. These four models are perturbed in different ways, evolved, and analyzed as described below.

Boson Star Configurations				
Model	$\phi(0)$	M	ω_0	R_{95}
1	0.1414	0.584	0.91	9.10
2	0.271	0.633	0.85	6.03
3a	0.3536	0.622	0.82	5.05
3b	0.300	0.631	0.84	5.65

Table 1. Physical characteristics of the boson star configurations studied in this paper are listed. The field ϕ is in units of $(1/\sqrt{4\pi})M_{\text{Pl}}$. The unperturbed mass M of the boson star is in units of M_{Pl}^2/m . The equilibrium scalar field frequency ω_0 is in units of m/M_{Pl}^2 and the radius R_{95} has units of M_{Pl}^2/m . By the radius of the boson star we are referring to the 95% mass radius of the star. M_{Pl} and m are the Planck mass and the mass of the scalar field, respectively.

All simulations presented in this paper are performed using octant symmetry. More general simulations on a full grid are the subject of future work. This will allow the study of the effect of using octant symmetry on the accuracy and stability of boson star simulations. The waveforms are calculated using the Cactus Extract module for the Zerilli function and the Cactus Psikadelia module for Ψ_4 with a radial tetrad

choice [21]. This particular wave extraction code has been widely used in the past [27, 28, 29, 30, 31, 32, 33].

The Newman-Penrose complex scalars Ψ_0 – Ψ_4 [34, 35] represent the ten independent components of the Riemann tensor projected onto a basis formed by a null tetrad. These scalars have asymptotic behavior $\Psi_n \sim r^{n-5}$. Thus, the scalar Ψ_4 dominates in the distant wave zone and approximates an outgoing gravitational wave.

The Zerilli function [36] is a gravitational waveform that is generated in the study of linear perturbations of the Einstein field equations. When the full system of the Einstein equations is expanded about a background Schwarzschild metric with a small perturbation function $h_{\mu\nu}$ (proportional to spherical harmonics $Y_{\ell m}$), the resulting linear equations contain a set describing even parity perturbations. For the Zerilli function ψ_Z , the energy loss to gravitational waves can be calculated using

$$E(t) = \frac{1}{32\pi} \int dt \left(\frac{\partial \psi_Z}{\partial t} \right)^2. \quad (16)$$

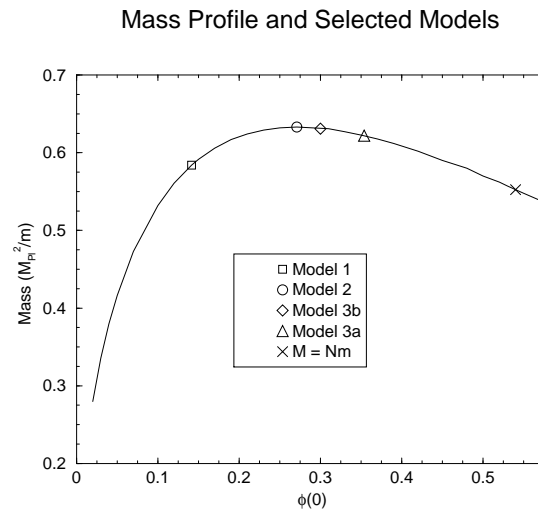


Figure 1. The mass versus central field density $\phi(0)$ for ground state boson star configurations is shown. The mass increases to a maximum of $0.633M_P^2/m$. This is the critical boson star configuration that separates the stable and unstable branches. The points shown in the curve correspond to the particular equilibrium configurations analyzed below.

3.1. Methods of Perturbation

Various initial data sets that represent different classes of nonspherical perturbations of boson star configurations are prepared. The equilibrium field configuration, spherically symmetric solution $\Phi(r)$, is taken as a base and different types of perturbations are added to this configuration. One method involved a scalar field perturbation of the form

$$\delta\Phi = \sum_{\ell m} \epsilon_{\ell m} Y_{\ell m}(\theta, \varphi) f(r) \Phi(r) \quad (17)$$

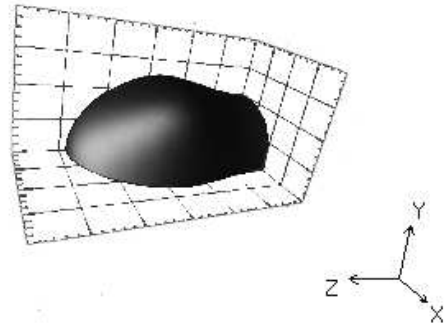


Figure 2. Conformal Factor isosurface $\Psi = 1.00001$ after the initial value problem solve. The perturbation of the field is proportional to the Y_{20} spherical harmonic. The dumb-bell shape of the harmonic is apparent in the shape of the conformal factor and thus in the initial corrections to the metric.

where $f(r)$ is a weighting function.

Various weighting functions were studied.

- Uniformly weighted: For this perturbation the weighting function was constant, $f(r) = 1$. In this case the scalar field was perturbed across the width of the star, and was of significant size near the origin where the field density ϕ is maximum.
- Parabolic weighted :

$$f(r) = \begin{cases} \left(\frac{r}{R_p}\right)^2 & r < R_p \\ 1 & r \geq R_p \end{cases} \quad (18)$$

(where R_p is a radius at which the perturbation is centered). In this case the perturbation is set to zero at the origin. This results in a more slight perturbation, away from the central peak of the field density of the star.

More general perturbations involved both radial and nonradial components. One such radial-nonradial (R-NR) perturbation type was constructed by giving full weight to a spherically perturbed profile along one direction, while keeping an unperturbed profile in the perpendicular directions and a smooth linear combination of the two in the intermediate region.

For all the perturbations described in this paper the metric functions are not explicitly perturbed. The initial value problem solver starts with the perturbed scalar field configuration described above and an initial guess for the metric functions and then solves the constraint Eq. (15) for the corrected metric functions. The initial guess for the metric functions is taken to be the usual spherically symmetric models of Ref. [12, 10, 11] obtained by solving a one-dimensional eigenvalue problem for time independent metric functions and for a field configuration oscillating with fixed frequency ω_0 and constant amplitude at the origin. These perturbations are similar to those performed by Ref. [13]. Alternative perturbations could involve external fields that evolve independently of the scalar field of the star (see Ref. [18]).

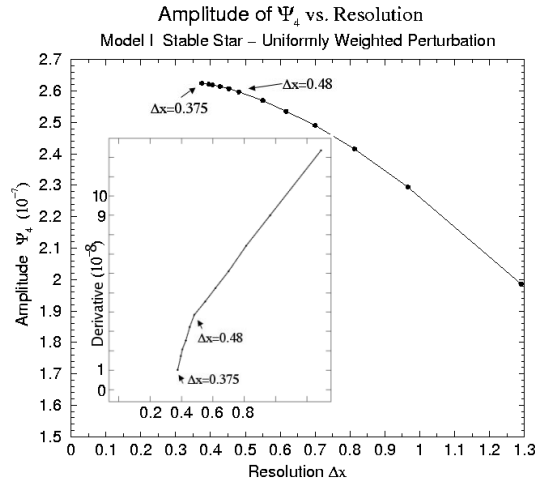


Figure 3. The amplitude of the Newman-Penrose scalar Ψ_4 is displayed as a function of resolution for a collection of simulations of a Model I stable star. In each simulation the waveform was extracted at a detector located at $r = 56.8$. The Ψ_4 amplitude of a given simulation is represented by black dot on the plot. The inset shows the first derivative of the amplitude curve. It can be seen that for a resolution better than $\Delta x = \Delta y = \Delta z = 0.48$ the curve flattens and its derivative goes sharply towards zero. A linear extrapolation towards infinite resolution shows the amplitude at $\Delta x = \Delta y = \Delta z = 0.375$ to vary from the continuum limit by only about 1-2%.

An example of the results obtained from the IVP solver is shown in Fig. 2. An isosurface of the conformal factor for a perturbation of the field proportional to the Y_{20} spherical harmonic is visualized. The prominent dumb-bell shape of the harmonic along the z -axis resurfaces in this display of the corrections to the initial metric.

3.2. Perturbation cases studied

3.2.1. ‘Pure’ nonspherical perturbations The evolution of boson stars under ‘pure’ nonspherical perturbations ($\delta M(r) \sim 0$ where δM is the mass change) that are proportional to spherical harmonics was investigated. Under such perturbations the quasinormal modes corresponding to nonradial oscillations were found to have frequencies with both real and imaginary parts [19] (even for configurations that are unstable or critical in nature with respect to spherical perturbations). Thus, it was anticipated that equilibrium boson star configurations would be stable with respect to nonspherical perturbations.

A series of simulations of perturbed star configurations was performed by taking different values for the coefficients $\epsilon_{\ell m}$ and the weighting function $f(r)$ in Eq. (17). These perturbations do not significantly change the mass of the star or the number of particles (even for a large nonspherical perturbation the mass change is less than 0.01%). The gravitational wave content is calculated using the even parity quadrupole ($\ell = 2$) Zerilli waveforms and the Newman-Penrose scalar Ψ_4 . The waveforms are

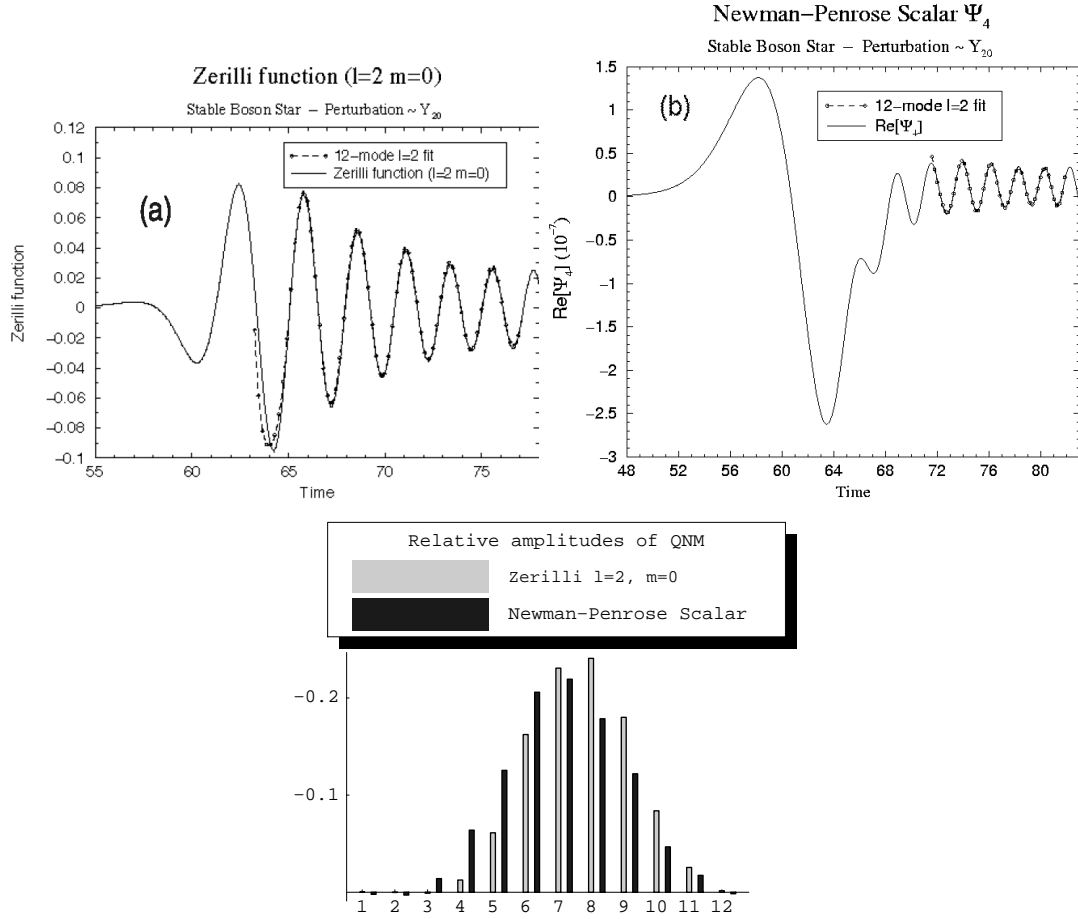


Figure 4. A stable boson star (Model 1, Table 1) is subjected to a small uniformly weighted perturbation proportional to Y_{20} with $\epsilon_{20} = 0.032$. (a) The Zerilli $\ell = 2, m = 0$ and (b) the Ψ_4 waveforms are shown in agreement with modefits (for time intervals [65.0, 79.2] and [71.6, 81.9], respectively) using the first twelve quasinormal modes of Ref. [19]. Both waveforms exhibit a low frequency precursor that likely represents the initial shaking of the star due to an instantaneous finite perturbation. Ψ_4 appears to be a more sensitive indicator of the initial dynamics of the star. (c) Coefficients of the modes for the two waveforms are shown to have similar profiles. The contribution of the first two modes is negligible, probably due to the failure of the WKB approximation in determining these modes accurately [19].

computed at several different detector locations in the spacetime. The detectors had to be located sufficiently far from the center of the star for the Ψ_4 scalar to dominate the other scalars in the Newman-Penrose formalism. Since the boson field tails off exponentially, the spacetime in the exterior regions ($r > R_{95}$) becomes increasingly close to Schwarzschild as the radius increases. The perturbation formalism associated with the Zerilli waveforms is valid when the metric functions describing the spacetime are only small perturbations away from those of the Schwarzschild spacetime. Thus detectors measuring Zerilli waveforms should be located at a distance greater than several R_{95} from the center of the star. Simultaneously, the detectors cannot be too close to the

boundary in order to avoid the effects of reflection from the edge of the grid. These two requirements coupled with computational limitations on the grid size and the need for good resolution are the main challenges of our numerical simulations.

A uniformly weighted perturbation was first considered. Two different perturbations were applied to a Model 1 (Table 1) stable configuration. One perturbation was proportional to the Y_{20} spherical harmonic with constant of proportionality $\epsilon_{20} = 0.032$. The second perturbation was a linear combination of Y_{20} and Y_{22} with coefficients of $\epsilon_{20} = 0.032$ and $\epsilon_{22} = 0.026$. In the beginning several simulations were performed to determine the scale of accurate grid resolution. Fig. 3 shows the amplitude of the real part of the Newman-Penrose Ψ_4 scalar for the same grid size at different resolutions for the stable star configuration under the perturbation proportional to Y_{20} described above. The waveform is extracted at a radial location of $r = 56.8$. From the figure it can be seen that at coarse resolution there is a strong dependence on amplitude. However, for resolutions better than $\Delta x = \Delta y = \Delta z = 0.48$ the curve flattens, with the slope heading rapidly towards zero. The amplitude at the best resolution $\Delta x = \Delta y = \Delta z = 0.375$ varies from an extrapolation to the infinite resolution limit by only about 1-2%. The final simulation was carried out on a 164^3 grid with a resolution of $\Delta x = \Delta y = \Delta z = 0.375$. The L2-norm of the Hamiltonian constraint for this run remained below 1.2×10^{-4} for the duration of the evolution. The L2-norm of the momentum constraints is about an order of magnitude lower than that of the Hamiltonian constraint with a maximum value of 4×10^{-5} .

Figs. 4(a) and (b) show the $\ell = 2, m = 0$ Zerilli function and the Newman-Penrose scalar Ψ_4 from a detector at $r = 56.8$. The plots also show a linear least squares regression using the first twelve $\ell = 2$ quasinormal modes calculated in Ref. [19]. It is observed that after an initial precursor, the star rings into a linear combination of its quasinormal modes. The waveforms are observed to be four orders of magnitude above the level of the noise, which is taken to be the signal obtained from a simulation of an unperturbed spherical star configuration with the same grid size and resolution. Although the perturbation of the field contains only $\ell = 2, m = 0$ spherical harmonics, it is observed that higher order $\ell = 4$ Zerilli modes of the gravitational radiation are also triggered. However, these Zerilli modes have sufficiently low amplitude (about an order of magnitude smaller than $\ell = 2$ modes) that they do not contribute significantly to the energy loss in gravitational radiation. The waveform Ψ_4 contains all nontrivial modes of the star. Nevertheless, the $\ell = 2$ modes dominate and we are able to fit the signal with the $\ell = 2$ frequencies determined by Ref. [19]. Using Eq. (16) the energy loss in gravitational waves was calculated to be about 0.1% of the mass of the star.

In Fig. 4(c) the relative weights of the twelve modes within the Zerilli and Ψ_4 waveforms for the stable star from Fig. 4(a) and (b) are shown. Both waveforms have roughly the same mode content. The slow increase of the imaginary part of the modes as the order of the mode increases necessitates the use of numerous modes in our fit. Note that in black hole systems, it is usually sufficient to fit waveforms dominated by quasinormal modes using only the lowest two modes [37]. In this case, however, it is

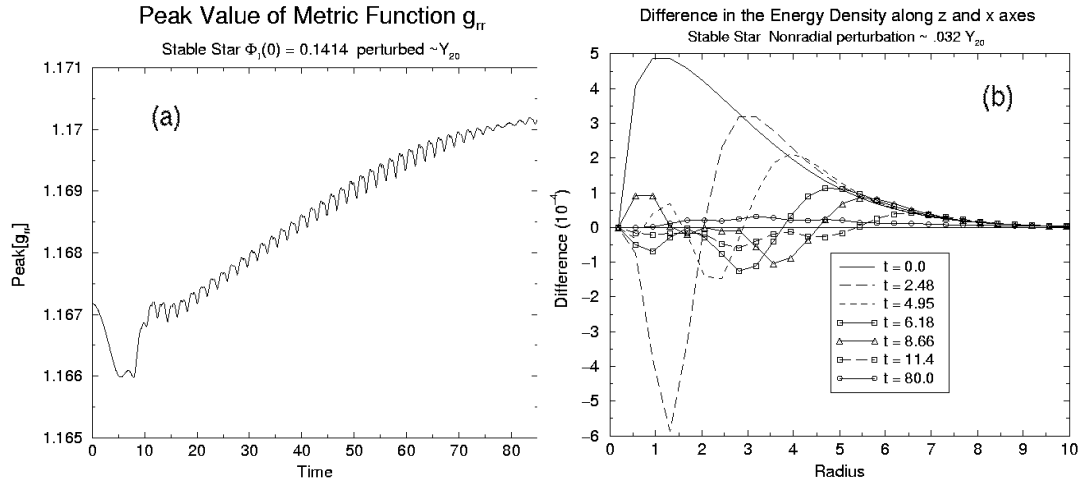


Figure 5. A Model 1 star is perturbed with a uniformly weighted perturbation proportional to Y_{20} with $\epsilon_{20} = 0.032$. Although no explicit radial perturbation was applied, numerical perturbations due to grid discretization (resolution $\Delta x = \Delta y = \Delta z = 0.375$) impose a slight radial perturbation on the system. The amplitude of this oscillation is seen to converge toward zero as the resolution is improved. (a) The maximum value of g_{rr} is plotted against time. As a result of the nonspherical perturbation the metric exhibits a high frequency oscillation superimposed on the low frequency one. By $t = 80$ the star has undergone only half of its radial oscillation, while the nonradial oscillations have damped off. (b) The difference between the density ρ in the x and z directions is shown as a function of time. This difference is an indicator of the degree of asymmetry in the system. It is clearly decreasing as the system evolves and the star becomes spherical after the relaxation of the nonradial modes.

justified to neglect only the modes beyond about twelve, on the grounds that by then the imaginary part is sufficiently large and they damp out quickly. As can be seen in the figure, even the 11th and 12th modes hardly contribute. It is noteworthy that the first two quasinormal modes are almost absent from the fit. However, these first modes have been described as inaccurate in Ref. [19] by the authors because of the break down of their WKB approximation in that domain. It should also be noted that values of the eigenfrequencies of Ref. [19] are dependent on their choice for a definition of the surface of the boson star. There is no unique definition for this radius, since the bosonic field extends to infinity with exponential damping. Hence, there is a degree of arbitrariness in the position of the surface and in the exact numerical values of the eigenfrequencies. In their work the surface of the star was artificially placed where the value of the field was of order 10^{-5} . We take more realistic field configurations, which are limited by the size of the grid and the resolution of our simulations.

The maximum of the radial metric function g_{rr} is shown in Fig. 5(a). The nonradial quasinormal mode oscillations are superimposed on the radial oscillation. The latter is introduced by grid discretization and its amplitude is resolution dependent. In the continuum limit one should observe only the high frequency oscillations. Ref. [20] has shown that the amplitude of the radial oscillation converges toward zero as the resolution

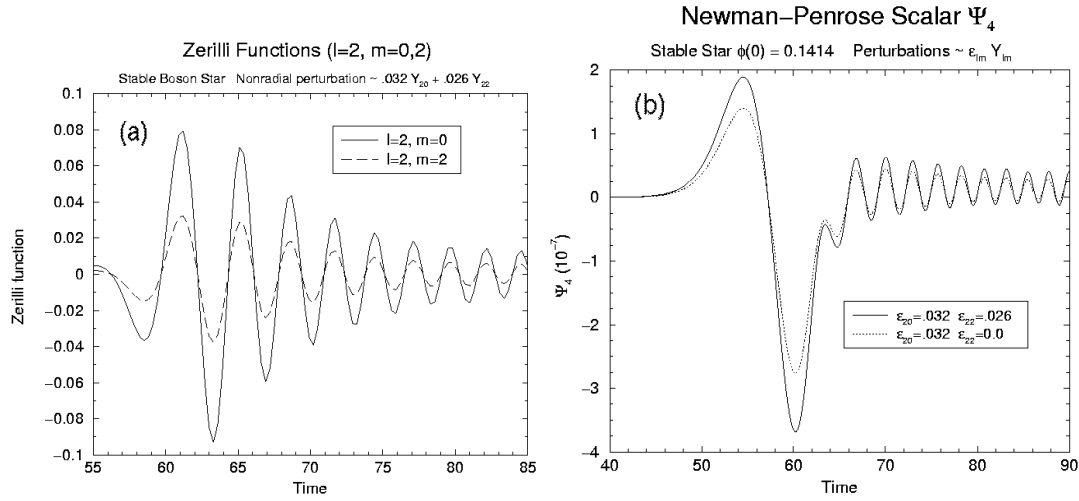


Figure 6. (a) Figure displaying the $\ell = 2$ Zerilli waveforms for a Model 1 stable star under a small uniformly weighted perturbation proportional to both the Y_{20} and Y_{22} spherical harmonics with amplitudes $\epsilon_{20} = 0.032$ and $\epsilon_{22} = 0.026$. The frequency of the Zerilli $\ell = 2, m = 2$ is identical to the frequency of the $\ell = 2, m = 0$ Zerilli. (b) The Ψ_4 waveform for the same star for the perturbation proportional to a linear combination of Y_{20} and Y_{22} is compared to the waveform for a Y_{20} perturbation with $\epsilon_{20} = 0.032$. The very similar frequencies indicate that this configuration has specific nonradial quasinormal mode signatures. It can be seen that the Ψ_4 signal for the mixed perturbation is larger because the Newman-Penrose scalar incorporates more modes.

is improved and that in the spherical case no high frequency oscillations appear. For this run at a resolution of $\Delta x = \Delta y = \Delta z = 0.375$, the maximum of the metric has risen only from about $g_{rr \max} = 1.166$ to $g_{rr \max} = 1.170$. The frequency of a radial oscillation of this star configuration was calculated for this simulation to be about $0.010 m/M_{\text{Pl}}^2$, which agrees with the result $\sim 0.0097 m/M_{\text{Pl}}^2$ obtained from a 1D code for the same configuration. Since the radial oscillation has a large time period, only half of this oscillation has occurred by the end of this run. The damping of the nonradial modes can be seen towards the end of the simulation, indicating that the star was settling into a spherical configuration. Another simulation that doubled the amplitude of the nonspherical perturbation ϵ_{20} was performed. It was observed that the amplitude of the nonradial oscillations in the metric g_{rr} also doubled. This is consistent with the result of Ref. [19] that the metric perturbation is comparable to the scalar field perturbation.

Fig. 5(b) shows the difference between the density ρ in the x and z directions as a function of time. This difference is seen to be decreasing by an order of magnitude in a short timescale. Furthermore, the radial location of the peak of the difference function is observed to be moving out as the star becomes more spherical, coinciding with the emission of gravitational radiation.

We now apply a different perturbation to Model 1 and study its evolution. In this case a uniformly weighted perturbation proportional to a linear combination of Y_{20} and Y_{22} (amplitudes $\epsilon_{20} = 0.032$ and $\epsilon_{22} = 0.026$, respectively) was applied. Fig. 6(a)

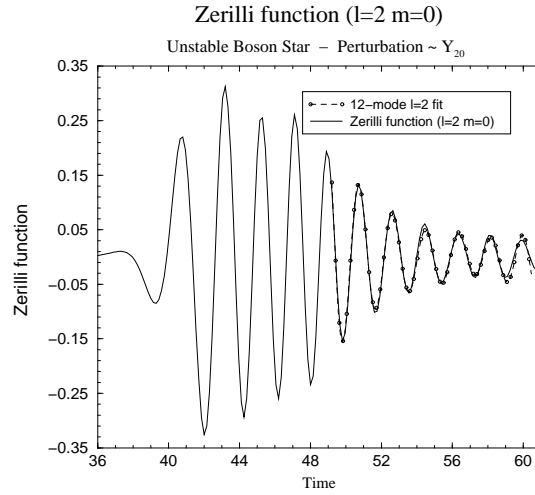


Figure 7. The Zerilli waveform for an unstable boson star (Model 3a, Table 1) under a small uniformly weighted perturbation proportional to the Y_{20} spherical harmonic ($\epsilon_{20} = 0.032$) is displayed. The waveform is shown along with modefit applied over the interval $[49.2, 60.5]$.

presents the extracted Zerilli $\ell = 2$ (both $m = 0$ and $m = 2$) waveforms for a stable star (Model 1, Table 1). These waveforms are observed to have the same frequency. Furthermore, the Zerilli $\ell = 2, m = 0$ signal for the star under this mixed Y_{20} and Y_{22} perturbation has the same size and frequency as the $\ell = 2, m = 0$ Zerilli function of the same star under a perturbation proportional only to Y_{20} (in both cases $\epsilon_{20} = 0.032$). This result shows that the addition of other harmonics to the perturbation does not alter the original signal and demonstrates the accuracy of the code. Fig. 6(b) shows a comparison between the Newman-Penrose scalars Ψ_4 for the pure Y_{20} perturbation and the mixed Y_{20} – Y_{22} perturbation. The signals have the same frequencies, but the signal for the mixed perturbation is larger in size because it incorporates more modes.

Perturbations proportional to the Y_{20} spherical harmonic with amplitude $\epsilon_{20} = 0.032$ were studied in the case of a critical boson star (Model 2, Table 1) and an unstable boson star (Model 3a, Table 1). Since these stars are more compact than the stable star, they need better resolution. However, they have a smaller radius and do not need the same grid size. A 164^3 grid with a resolution of $\Delta x = \Delta y = \Delta z = 0.25$ was used for both these simulations. For the time interval relevant to our study (that prior to and encompassing waveform extraction) the simulations proceed accurately with the L2-norm of the Hamiltonian constraint remaining below 4.6×10^{-4} for the critical case and below 6.1×10^{-4} for the unstable case, respectively. At late times both stars collapse to black holes due to radial perturbations introduced by grid discretization errors. More detailed simulations of unstable star collapse with apparent horizon analysis are presented in Sec. 3.3. Fig. 7 displays the $\ell = 2, m = 0$ Zerilli waveform and modefit for this unstable star configuration with a detector located at $r = 35$. After a fairly large precursor, the star settles into a linear combination of its quasinormal modes with late

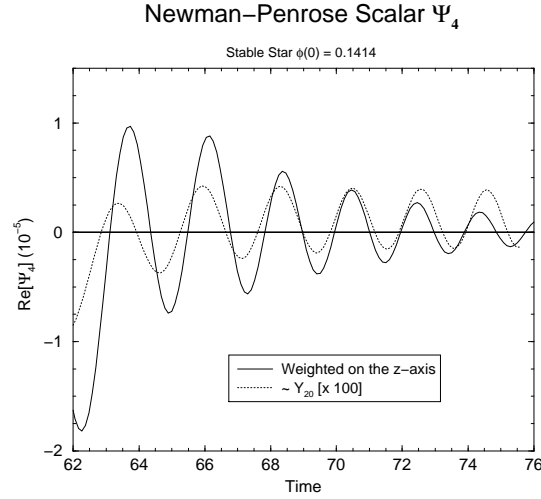


Figure 8. Newman-Penrose scalar Ψ_4 for a Model 1 star under a R-NR perturbation is superimposed on the signal due to the Y_{20} perturbation shown in Fig. 4(b). The amplitude of the latter has been magnified by a factor of 100 to facilitate the comparison. The R-NR perturbation produces a much larger signal. The star did not ring in its quasinormal modes initially, but appears to move into these modes after a few oscillations. The rapid damping of the gravitational wave signal characteristic to boson stars can be clearly seen.

time agreement between the modefit and numerical waveforms. The extended precursors are representative of complex dynamics within unstable systems.

3.2.2. Perturbation weighted along a chosen axis Perturbations with radial and nonradial components as described in Sec. 3.1 were also studied. In Ref. [7] it was shown that for this type of perturbation the dominant radiation is in the form of scalar radiation. The scalar radiation emission process, denoted gravitational cooling [38], relaxes the system to an equilibrium configuration. In this case the Zerilli waveform appeared noisy and did not exhibit the quasinormal mode oscillation. The Zerilli perturbation expansion about a background Schwarzschild spacetime was probably affected when scalar radiation moved through the region of the detector. Even when the initial configuration has the detector in an almost Schwarzschild region, the dynamics of the star can push scalar radiation into this region during the evolution. The Newman-Penrose scalar was observed to be more robust in the presence of scalar radiation.

Fig. 8 shows the Ψ_4 waveform for this perturbation for a Model 1 boson star superimposed on the waveform for the same star under the Y_{20} perturbation of Fig. 4(b). The R-NR simulation was conducted on a 164^3 grid with resolution $\Delta x = \Delta y = \Delta z = 0.35$. Since the Y_{20} perturbation is significantly smaller, it gives a much smaller signal. In order to make a clear comparison the waveform for the Y_{20} perturbation has been magnified by a factor of 100. Although the R-NR perturbation is not huge, it is large enough to prevent the star from ringing into its quasinormal modes initially.

However, it appears to move into these modes after a few oscillations as can be seen in the figure. The oscillation is very clearly damping out on a short timescale as it is characteristic for boson stars [19].

3.3. Unstable Star Collapse to a Black Hole

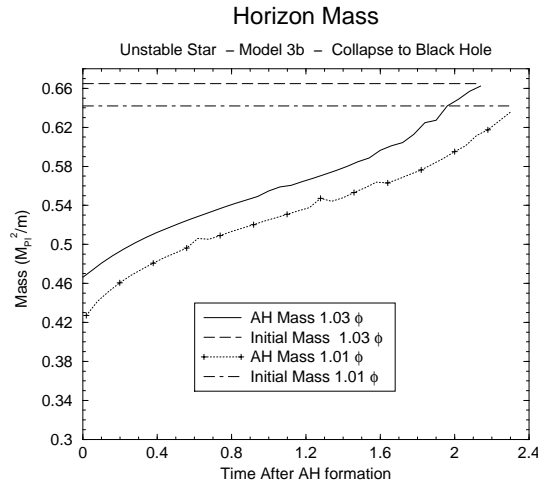


Figure 9. The mass of the apparent horizon vs. the time elapsed after horizon formation is displayed for star collapse simulations Run 1 and Run 2 described in the text. Run 1 has an amplification factor of 1.01 and an initial mass of $M = 0.642M_{P1}^2/m$. Run 2 has radial amplification factor of 1.03 and initial mass $M = 0.665M_{P1}^2/m$. In each case the horizon mass is observed to steadily increase towards the total mass of the initial configuration as more scalar matter falls through the horizon surface. An asymptotic approach to the value of the initial mass is expected and is observed at early times, but large errors due to grid stretching cause the mass to rise quickly at late time.

In this section simulations that follow the collapse of unstable boson stars under nonspherical perturbations to the formation of black hole horizons are presented. The unstable star designated as Model 3b in Table 1 is used as the starting configuration. A parabolic weighted nonradial perturbation centered at $R_p = 2.5$ (about half of the 95% radius of the unstable star) was applied. This nonradial perturbation was superimposed on different radial perturbations that accreted additional matter onto the star by means of a uniform amplification of the field of the form $\mu \phi_{eq}$ (where $\phi_{eq}(r)$ is the initial equilibrium field configuration). The addition of scalar matter by a spherical amplification hastens the collapse process. In contrast, the star is observed to collapse at approximately the same rate with or without the nonradial perturbation.

The time dependence of the mass of the apparent horizon for two collapse simulations is displayed in Fig. 9. The nonspherical perturbations for the systems are parametrized by $\epsilon_{20} = 0.128$ and $\epsilon_{22} = 0.104$ (using Eq. (17)). The first simulation, denoted Run 1, has a radial amplification of $\mu = 1.01$ while the second, denoted Run 2, has a radial amplification of $\mu = 1.03$. For these amplifications the mass of the star

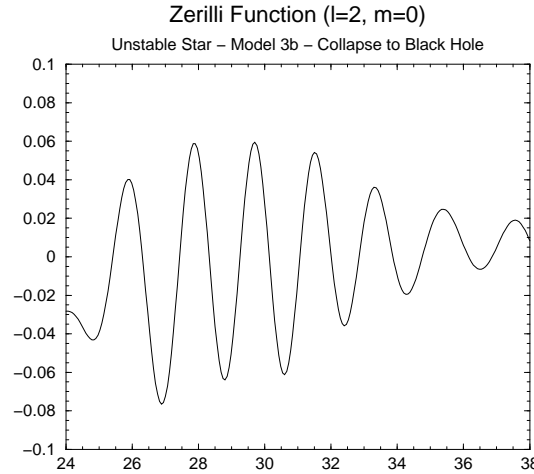


Figure 10. The $(\ell = 2, m = 0)$ Zerilli waveform for the case of the unstable star of Model 3b with amplification factor of $\mu = 1.03$ and nonradial perturbation specified by $\epsilon_{20} = 0.128$ and $\epsilon_{22} = 0.104$.

changes to $M = 0.642M_{\text{Pl}}^2/m$ for the $\mu = 1.01$ case (an increase of about 1.7% from the unperturbed mass) and $M = 0.665M_{\text{Pl}}^2/m$ for the $\mu = 1.03$ case (an increase of about 5.4% from the unperturbed mass). The horizon is observed to form at a time of $t = 38.3$ within Run 2. This is earlier than the formation time of $t = 54.7$ in Run 1, which is appropriate because of the larger initial mass. It can be seen that the horizon mass is $0.463M_{\text{Pl}}^2/m$ when first detected for the case of Run 2. The evolution is carried forward for an additional time interval $t = 2.1$ after horizon formation, corresponding to approximately $t = 3M$ of evolution of the black hole. A smooth asymptotic approach towards the value of the initial mass is observed at early times after the formation. However, at late times the errors in the simulation are becoming large and this is manifested in a slight upward turn of the curve along a path that would apparently cross the axis corresponding to the initial mass. These features are also echoed in the results for Run 1, where the mass of the apparent horizon takes the value $0.427M_{\text{Pl}}^2/m$ at formation and increases in an analogous manner. The late time errors are caused by the familiar problem of grid stretching associated with singularity avoiding time slicing [39, 40, 41]. It should be noted that these simulations did not make use of advanced shift conditions or excision techniques. Future work will include the employment of such methods to extend the duration of the simulations for long times after the black hole formation.

The geometry of the apparent horizons formed in Run 1 and Run 2 is investigated by calculating the ratio of the polar to equatorial circumference $C_r = C_p/C_e$ for two different great circles $\varphi = 0$ and $\varphi = \pi/2$. The values for $C_r(\varphi = 0)$ and $C_r(\varphi = \pi/2)$ are very close to unity, with values in the range $C_r = 0.9998 \pm 0.0002$ on all timesteps for which horizons are detected in the simulations. The nearly spherical shape of the horizons can be understood by considering the Zerilli waveform of Run 2 displayed

in Fig. 10. The waveform starts to ring down near $t = 30$ and damps to a small value by $t = 38$, which precedes the formation time of the apparent horizon within the simulation. The nonradial perturbations have decayed away and the system has become nearly spherical by the time of horizon formation. However, it can be demonstrated that a slightly nonspherical horizon may be obtained when the formation occurs before the full relaxation of the nonradial modes. Another simulation, Run 3, takes an initial configuration with a very large amplification factor $\mu = 1.15$ and the same nonradial coefficients ($\epsilon_{20} = 0.128, \epsilon_{22} = 0.104$) as Runs 1 and 2. The initial mass of this configuration is $0.801M_{\text{Pl}}^2/m$, and the subsequent evolution results in a horizon formed by $t = 20.5$. From the values of the circumference ratios displayed in Table 2 it is seen that

AH circumference ratios	
$t_{\text{formation}}$	t_{end}
$C_r(\varphi = 0) = 1.0017$	$C_r(\varphi = 0) = 1.0008$
$C_r(\varphi = \frac{\pi}{2}) = 1.0009$	$C_r(\varphi = \frac{\pi}{2}) = 1.0004$

Table 2. The ratios of the polar to the equatorial circumference for two different great circles ($\varphi = 0$ and $\varphi = \pi/2$) are displayed at the horizon formation time and at the end of Run 3. The termination time is $t_{\text{end}} = t_{\text{formation}} + 3.2 \approx t_{\text{formation}} + 4M$, where the apparent horizon forms at the time $t_{\text{formation}} = 20.5$.

the horizons are measurably nonspherical. The circumference ratios are seen to steadily decrease, suggesting the eventual evolution towards spherical symmetry. Furthermore, we see that the perturbation proportional to Y_{22} has resulted in a dependence in the ratio C_r on the angle φ at which the polar circumference is measured. The formation and study of horizons with complex shape from boson star collapse will be investigated further by using advanced methods for the evolution of black holes.

3.4. Migration from the Unstable Branch

A boson star on the unstable branch can migrate to a new configuration of smaller central field density that lies on the stable branch. This behavior is analogous to the behavior of relativistic neutron stars [42]. In both cases there is a large initial expansion of the star followed by oscillations about the final stable star configuration it will settle into. In the case of boson stars these oscillations damp out slowly, similar to the case of stars with a perfect fluid equations of state. The neutron star with perfect fluid equation of state settles into a configuration on the stable branch of slightly lower mass than the initial unstable star. The initial zero temperature star is heated due to gravitational binding energy being converted to internal energy by shock heating. The boson star on the other hand loses mass to scalar radiation and settles to a configuration of lower mass on the stable branch.

The mass of a critical boson star (Model 2, Table 1) was lowered by about 3.5% through a radial perturbation. This large perturbation reduced the boson

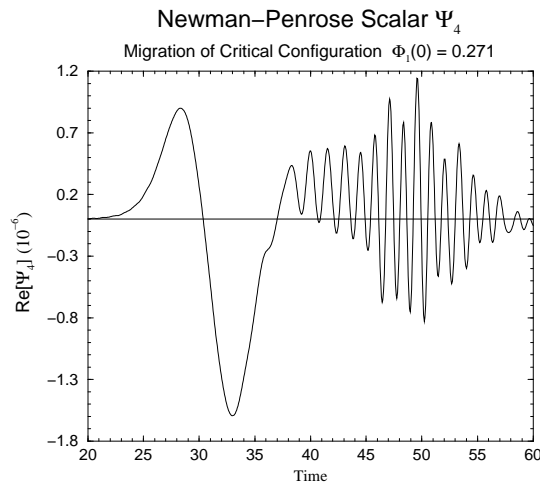


Figure 11. The Newman-Penrose waveform Ψ_4 is shown for a migrating critical star (Model 2). The initial mass of the unperturbed star was $0.633M_{\text{Pl}}^2/m$ and after a perturbation of the form $\Phi(r) \rightarrow 0.98\Phi(r)$ was lowered to $0.611M_{\text{Pl}}^2/m$. On top of this spherical perturbation a nonradial parabolic weighted perturbation proportional to $0.016 Y_{20}$ was applied. This was centered at about half the radius of the critical star. A grid size of 164^3 with resolution $\Delta x = \Delta y = \Delta z = 0.2$ was used. This waveform is significantly different from the nonradial quasinormal modes of a critical star. This is expected since the large initial perturbation moved the star significantly away from the original critical configuration. Subsequently it migrated to the stable branch, moving it further away from its initial configuration.

field everywhere to 98% of its original value. Next, a nonradial parabolic weighted perturbation (see Sec. 3.1) was superimposed on the radial one. The weighted perturbation was centered at a radius of $R_p = 3.025$, which is about half the 95% radius of the star. This was a pure Y_{20} perturbation with $\epsilon_{20} = 0.016$ in Eq. (17). The data was then passed through the IVP and its evolution was tracked using the 3D code.

The strong dynamics within the simulation causes substantial coordinate drifting. A dense unstable configuration with a small radius requires good resolution. This star migrates to a dilute stable configuration with a larger radius (about twice as large). The different scales place demands on both the resolution and gauge choice within the simulation. The gauge control was obtained by enforcing maximal slicing through a K-driver restoring term. When K is perturbed away from zero, this term drives it back exponentially in time [26]. For computational efficiency, the enforcement of maximal slicing is performed intermittently, with the algebraic 1+log slicing condition used on intermediate timesteps. While some gauge drift persists the coordinates within the simulation are stable. Future work will involve studying better gauge control through an adaptive mesh refinement technique [43].

Fig. 11 shows Ψ_4 at a detector at $r = 30$. The star is dynamic and moves away from the initial state even in the short damping timescale of the gravitational wave signal. Hence, the gravitational wave does not carry the signature of the original configuration.

The migration process to a stable star is an extremely lengthy process, and the waveform shown is emitted during the very early stage of this process. Thus, the waveform does not show the quasinormal modes of the eventual final state stable star or the initial critical configuration, but rather a complex combination of the modes of a mixture of states that the system goes through during the migration. A good modefit of this data with the quasinormal modes of any single star configuration is therefore not possible. The lengthily and complicated precursor (both low and high frequency parts) is indicative of the complex dynamics of the strong perturbation and migration process. A Fourier analysis of this waveform in the ring down region results in a dominant frequency of $4.3 m/M_{\text{Pl}}^2$. This frequency is reflective of the dynamics of the star under a strong perturbation, which does not result in excitation of quasinormal modes. It is much higher than any of the quasinormal modes of a critical star (as determined by Ref. [19]).

Since the detectors have to be far away for Ψ_4 to represent the gravitational signature of the star, a large grid had to be used to obtain the waveform. A very long run with such a grid would be computationally expensive. However, due to the strong damping of these waves, one can see the full gravitational ringing of the star on a short time scale ($t = 60$ for this simulation). On the other hand, if one wants to see the star continue its migration for a few radial oscillations, a longer run needs to be conducted. The period of one radial oscillation for this configuration is a lot larger than the damping time of the gravitational wave (almost four times as large). A two pronged approach was used. A shorter run with a large grid (164^3 of resolution $\Delta x = \Delta y = \Delta z = 0.2$) was performed to obtain the gravitational wave. Subsequently, a smaller grid (96^3 of resolution $\Delta x = \Delta y = \Delta z = 0.2$) was used to handle the migration. This was compared to a spherical perturbation run with the same grid and resolution.

The simulation proceeds accurately for several hundred oscillations of the underlying scalar field, with the L2-norm of the Hamiltonian constraint on the grid persisting at a value of order 10^{-4} at late times. At the time at which the simulation is stopped, it has not reach an error prone state at which it must be terminated, but rather we simply exhaust our available computer time. By all available indicators, the simulation would continue further at this level of accuracy. The level of the errors in our migration study compares very favorably to other published work. 3D numerical simulations by Font *et al.* [42] follow long-term evolutions of relativistic neutron stars and show errors that grow to a level of 10^{-2} by the end of the simulation. The constraint values we report persist at least an order of magnitude below this level for hundreds of oscillations of the underlying scalar field, the relevant time scale for our problem.

Fig. 12 shows the maximal radial metric g_{rr} as a function of time for a migrating (Model 2) critical star. The initial drop in the metric indicates a migration to the stable branch. The star then oscillates about the new stable configuration that it will settle into with the radial oscillations damping out slowly. The star settles into a fairly constant oscillation frequency. The last four peaks are at $t = 909, 1135, 1361$, and 1587 , all separated by $\Delta t = 226$. The metric in Fig. 12 also exhibits a shift upwards. We believe this a nonphysical effect, likely a result of gauge drift that occurs in response to

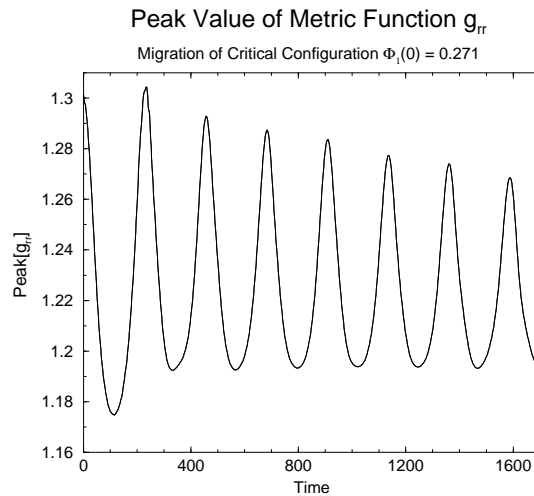


Figure 12. The maximum value of metric function g_{rr} is plotted against time for the migration of a critical star to the stable branch. The initial mass of the star was $0.633M_{\text{Pl}}^2/m$ and after a perturbation of the form $\Phi(r) \rightarrow 0.98\Phi(r)$ was lowered to $0.611M_{\text{Pl}}^2/m$. The nonradial oscillations have damped out early on (approximately by time $t = 60$) and the remaining spherical oscillations proceed through seven periods within this simulation. The frequency is very steady by the end with the last four peaks at $t = 909, 1135, 1361$, and 1587 , all separated equally by $\Delta t = 226$. A 96^3 grid of resolution $\Delta x = \Delta y = \Delta z = 0.2$ was used.

the very large initial perturbation. One can roughly estimate the final configuration to which the star will settle. The final star configuration of mass $0.59M_{\text{Pl}}^2/m$ corresponds to a maximum metric of $g_{rr \text{ max}} = 1.18$.

Since the star expands to a configuration of larger radius the grid size had to accommodate this expansion. This was at the expense of the grid resolution of the initial denser, more compact configuration. Similar problems were seen for neutron star simulations. In the neutron star case a 96^3 grid was used to study the migration and the low grid resolution of the initial configuration caused a nonnegligible deviation of the average central rest mass density from the expected value [42]. We plan to investigate the use of fixed mesh refinement [43] to accommodate the multiple length scales that occur within such migration studies.

In the nonradial perturbation case the high frequency oscillations, associated with the nonradial modes, of the peak of the metric function g_{rr} are superimposed on the low frequency radial oscillation. This superposition is not clear in the figure because the small amplitude of nonspherical oscillation is suppressed by the larger spherical oscillation amplitude. The spherical oscillation amplitude is of order 0.1. This is much larger than the corresponding radial oscillation amplitude due to discretization errors (of order 0.003) from Fig. 5(a) for the same timescale. While the nonspherical oscillation can not readily be seen, the metric exhibits the same superposition of the radial and nonradial frequencies discussed in Fig. 5(a).

4. Conclusion

This is the first paper to present the long time evolutions of boson stars under nonradial perturbations in full 3D general relativity. The existence of rapidly damping quasinormal modes as discussed by Ref. [19] is confirmed. For the first time gravitational waveforms (both Zerilli and Newman-Penrose scalar Ψ_4) have been fully extracted and presented for boson stars in 3D. We find that when a small nonradial perturbation is applied to a boson star, the star loses mass through gravitational radiation and has quasinormal modes frequencies that are much higher than its radial quasinormal mode frequency. The metric acquires this frequency signature. If the small nonradial perturbation in the scalar field is doubled the metric perturbation also doubles. For perturbations that have radial and nonradial components the metric exhibits both frequencies superimposed on one another. The gravitational wave signal is observed to damp out quickly and the star becomes spherical on a short timescale.

In this paper, the gravitational waveforms have been presented for stable, critical and unstable boson star configurations. Our results were compared to linear perturbation results of Ref. [19]. However, the comparison could only be approximate because their WKB formulation leads to inaccuracy for the calculation of the lowest modes. Furthermore, the calculation of the quasinormal frequencies in Ref. [19] is slightly dependent on the choice of the surface of the star. In principle, a boson star is of infinite extent with exponential damping of the scalar field within a short radius. This exponential damping allows one to consider a large part of the star to be virtually a vacuum and arbitrarily choose a surface somewhere in this region for calculational (perturbation theory) or numerical (finite grid) purposes. Different choices of surface can lead to slightly different results for the modes (changes them within a few percent).

We have considered perturbations that are purely nonradial and are proportional to the spherical harmonics. The Zerilli gravitational waveforms of the $\ell = 2, m = 0$ mode for small perturbations proportional to Y_{20} have the same frequencies as waveforms generated from perturbations composed of a linear combination of Y_{20} and Y_{22} for a given star configuration. This shows that a given star has a specific quasinormal mode signature.

It is more challenging to obtain gravitational waveforms when matter is present in the spacetime. Even if the system has an approximate Schwarzschild exterior region the dynamics of the simulation might carry matter there. The presence of matter can affect the Zerilli waveform which requires a region that is close to Schwarzschild. This effect was tested explicitly by using different types of perturbations. The first was purely nonradial, while the second was more general and had radial and nonradial components. The former did not result in scalar radiation and the Zerilli waveform was observed to exhibit the high frequency quasinormal mode oscillation, while the waveform in the latter case was noisy and seemed affected by the presence of scalar radiation. The Newman-Penrose waveforms behaved better in all cases.

Nonspherical apparent horizons were observed under nonradial perturbations when

the horizon formed before the full emission of the gravitational waveform. Radial perturbations that amplify the mass of the star are seen to accelerate the collapse. However, the nonradial perturbations do not affect the collapse time. The geometry of the horizon is seen to become more spherical as the star evolves. Even for large nonradial perturbations the degree of asymmetry is quite small.

Under large radial perturbations that mimic the removal of scalar field, an unstable branch star can migrate to the stable branch [12]. A large radial perturbation of an unstable star was performed for the first time in 3D and several oscillations of the metric were observed with the star settling to a constant oscillation frequency. This is a dynamic problem that involves multiple scales. Gauge control was obtained using a stable implementation of maximal slicing. Improvements are under study. A nonradial perturbation superimposed on the radial perturbation resulted in the emission of gravitational waves during the migration. The migration of an unstable branch star to the stable branch under a general perturbation (with both radial and nonradial components) can be significant in the formation of boson stars [12].

Acknowledgments

We thank Jason Ventrella and Manuel Tiglio for the careful review of our manuscript. Our code is fully based on the Cactus Computational Toolkit. We gratefully acknowledge the Cactus team for their help and extensive support, particularly Thomas Radke. We want to especially thank Gabrielle Allen for her assistance and overall guidance. We would like to recognize Erik Schnetter for developing the Cactus TAT interface to the PETSc elliptic solver that is used by our IVP solver. We thank Jian Tao, Malcolm Tobias, and Wai-Mo Suen for useful conversations and access to Washington University computer resources. J.B. would like to especially thank Matt Visser for helpful discussions and encouragement for this project. R.B. is grateful to Doina, Cornel, Ileana and Ruxandra Costescu for their hospitality and support during the length of this project. The large-scale computations were performed on the Platinum and Tungsten clusters at NCSA under the NSF NRAC grant MCA02N014 and on the SuperMike cluster at LSU. We thank LSU CCT for their well-organized visitor program. We also acknowledge generous support from Microsoft. F. S. G. and E. S. acknowledge partial support from the bilateral project DFG-CONACYT 444 MEX-13/17/0-1. F.S.G. is partly granted by CIC-UMSNH-4.9 and PROMEP-UMICH-PTC-121.

References

- [1] A. H. Guth, *Phys. Rev. D* **23** (1981) 347. A. D. Linde, *Phys. Lett. B* **108** (1982) 389. R. Brandenberger, *Rev. Mod. Phys.* **57** (1985) 1.
- [2] R. R. Caldwell, R. Dave and P. J. Steinhardt, *Phys. Rev. Lett.* **80** (1998) 1582. I. Zlatev, L. Wang and P. J. Steinhardt, *Phys. Rev. Lett.* **82** (1999) 896. P.J. Steinhardt, L. Wang and I. Zlatev, *Phys. Rev. D* **59** (1999) 123504.

- [3] E. Seidel and W.-M. Suen, Phys. Rev. Lett. **66**, 1659 (1991). M. Alcubierre et al. Class. Quantum Grav. **20** 2883-2904 (2003). L. A. Ureña López, Class. Quantum Grav. **19**, 2617-2632 (2002).
- [4] Jae-weon Lee, In-guy Koh, Phys. Rev. **D 53** (1996) 2236. E. W. Mielke and F. E. Schunck, Phys. Rev. **D 66** (2002) 023503. F. S. Guzmán and L. A. Ureña-López, Phys. Rev. **D 68** (2003) 024023.
- [5] D. F. Torres, S. Capozziello, G. Lambiase Phys. Rev. **D 62** (2000) 104012
- [6] F. S. Guzman, Phys. Rev. D. **73**, 021501(R) (2006).
- [7] J. Balakrishna, Ph.D. Thesis, Washington University 1999. E-version: gr-qc/9906110.
- [8] F. D. Ryan, Phys. Rev. D. **55**, 6081 (1997).
- [9] M. Kesden, J. Gair and M. Kamionkowski, Phys. Rev. D **71**, 044015 (2005).
- [10] R. Ruffini and S. Bonazzola, Phys. Rev. **187** (1969) 1767.
- [11] D. J. Kaup, Phys. Rev. **172** (1968) 1331.
- [12] E. Seidel and W.-M. Suen, Phys. Rev. D. **42**, 384 (1990).
- [13] J. Balakrishna, E. Seidel, W.-M. Suen, Phys. Rev. D. **58** 104004 (1998).
- [14] M. Gleiser, Phys. Rev. D **38**, 2376 (1988); **39**, 1257 (E) (1989).
- [15] T. D. Lee, Phys. Rev. D **35**, 3637 (1987).
- [16] P. Jetzer, Phys. Rep. **220**, 183 (1992).
- [17] F. E. Schunck and E. W. Mielke, Class. Quantum Grav. **20**, R301 (2003).
- [18] S. H. Hawley and M. Choptuik, Phys.Rev. **D62** (2000) 104024.
- [19] S. Yoshida, Y. Eriguchi, T. Futamase, Phys. Rev. D. **50**, 6235 (1994).
- [20] F. S. Guzman, Phys. Rev. **D 70**, 044033 (2004).
- [21] <http://www.cactuscode.org>
- [22] M. Alcubierre, B. Breugmann, T. Dramlitsch, J. A. Font, P. Papadopoulos, E. Seidel, N. Stergioulas, R. Takahashi, Phys. Rev. D **15**, 62, 124011, (2000).
- [23] T. W. Baumgarte, S. L. Shapiro, Phys. Rev. D **59**, 024007 (1998). M. Shibata, T. Nakamura, Phys. Rev. D **52**, 5428 (1995).
- [24] M. Alcubierre, F. S. Guzmán, T. Matos, D. Núñez, L. A. Ureña-López and P. Wiederhold, Class. Quantum Grav. **19**, 5017 (2002).
- [25] S. Teukolsky, Phys. Rev. D **61**, 087501 (2000).
- [26] J. Balakrishna, G. Daues, E. Seidel, W.-M. Suen, M. Tobias, E. Wang, Class. Quantum Grav. **13**, L135-L142 (1996).
- [27] M. Alcubierre, B. Bruggmann, D. Pollney, E. Seidel, and R. Takahashi, Phys.Rev. D **64**, 61501 (2001).
- [28] M. Alcubierre, W. Benger, B. Bruggmann, G. Lanfermann, L. Nerges, E. Seidel and R. Takahashi, Phys.Rev.Lett. **87** , 271103 (2001), gr-qc/0012079.
- [29] S. Brandt, J.A. Font, J.M. Ibanez, J. Masso, E. Seidel, Comput.Phys.Comm. **124**,169-196 (2000).
- [30] G. Allen, K. Camarda, E. Seidel, gr-qc/9806014. K. Camarda, E. Seidel, Phys.Rev. D **57**, 3204 (1998). K. Camarda, E. Seidel, Phys.Rev. D **59**, 064019 (1999).
- [31] P. Anninos, R. H. Price, J. Pullin, E. Seidel, and W.-M. Suen, Phys.Rev. D **52**, 4462 (1995).
- [32] A. Abrahams, D. Bernstein, D. Hobill, E. Seidel, and L. Smarr, Phys. Rev. D **45**, 3544 (1992).
- [33] J. Baker, M. Campanelli, C. O. Lousto, Phys. Rev. D **65**, 044001 (2002), gr-qc/0104063.
- [34] E. T. Newman, R. Penrose, J. Math. Phys. **3**, 566 (1962).
- [35] R. Penrose, Phys. Rev. Lett. **10**, 66 (1963).
- [36] F. J. Zerilli, Phys. Rev. D, **2**, 2141 (1970).
- [37] P. Anninos, D. Hobill, E. Seidel, L. Smarr, W.-M. Suen, Phys.Rev. D **52**, 2044 (1995).
- [38] Seidel and W.-M. Suen, Phys. Rev. Lett. **72**, 2516 (1994). F. S Guzmán and L. A Ureña-López, Phys. Rev. **D 69** 124033 (2004).
- [39] L. Smarr, Ann. N.Y. Acad. of Sciences **302**, 569, (1977).
- [40] P. Anninos, G. Daues, J. Masso, E. Seidel, W.-M. Suen, Phys. Rev. D. **51**, 5562 (1995).
- [41] P. Anninos, K. Camarda, J. Masso, E. Seidel, W.-M. Suen, J. Town, Phys. Rev. D. **52**, 2059 (1995).

- [42] J. Font, T. Goodale, S. Iyer, M. Miller, L. Rezzolla, E. Seidel, N. Stergioulas, W.-M. Suen and M. Tobias, Phys. Rev. D, **65** 084024 (2002).
- [43] E. Schnetter, S. H. Hawley and I. Hawke, Class. Quantum Grav. **21**, 1465 (2004).
<http://www.carpetcode.org>